Geochemistry Geophysics Geosystems G3

Article
Volume 12
28 January 2011
Q0AD06, doi:10.1029/2010GC003284
ISSN: 1525-2027

Published by AGU and the Geochemical Society

Quantification of free gas in the Kumano fore-arc basin detected from borehole physical properties: IODP NanTroSEIZE drilling Site C0009

Mai-Linh Doan
Institut des Sciences de la Terre, CNRS, Université Joseph Fourier, BP 53, F-38041 Grenoble CEDEX 9, France (Mai-Linh.Doan@obs.ujf-grenoble.fr)

Marianne Conin and Pierre Henry
Université Aix-Marseille III, CNRS, CEREGE, Europole de l'Arbois, BP 80, F-13545 Aix en Provence, France

Thomas Wiersberg
Helmholtz Zentrum Potsdam, Deutsches GeoForschungsZentrum, Section 4.2, Telegrafenberg, D-14473 Potsdam, Germany

David Boutt
Department of Geosciences, University of Massachusetts Amherst, 611 North Pleasant Street, 233 Morrill Science, Amherst, MA 01003, USA

David Buchs
Research School of Earth Sciences, The Australian National University, 61 Mills Road, Building J1, Canberra, ACT 0200, Australia

Demian Saffer
Geosciences, Pennsylvania State University, 310 Deike Building, University Park, PA 16802, USA

Lisa C. McNeill
National Oceanography Centre, Southampton, University of Southampton, European Way, Southampton SO14 3ZH, UK

Deniz Cukur
Department of Energy Resources Engineering, Pukyong National University, 599-1, Daeyeon 3-Dong, Nam-Gu, 608-737 Busan, South Korea

Weiren Lin
Kochi Institute for Core Sample Research, JAMSTEC, Monobe-otsu 200, Nankoku 783-8502, Japan

[1] The Kumano fore-arc basin overlies the Nankai accretionary prism, formed by the subduction of the Philippine Sea Plate beneath the Eurasian plate offshore the Kii Peninsula, SW Honshu, Japan. Seismic surveys and boreholes within the framework of the Nankai Trough Seismogenic Zone Experiment (NanTroSEIZE) project show evidence of gas hydrates and free gas within the basin. Here we use high-quality borehole sonic data from Integrated Oceanic Drilling Program (IODP) Site C0009 to quantify the free gas distribution in the landward part of the basin. The Brie theory is used to quantify gas content from sonic logs, which are calibrated from laboratory measurements on drill cores. First, we show that the sonic data are

mainly sensitive to the fluid phase filling the intergranular pores (effective porosity), rather than to the total porosity that includes water bound to clay minerals. We then compare the effective porosity to lithodensity-derived porosity that acts as a proxy for total porosity. The combination of these two data sets also allows assessment of clay mineralogy of the sediments. Second, we compute free gas saturation and find a gas-rich interval that is restricted to a lithological unit characterized by a high abundance of wood fragments and lignite. This unit, at the base of the fore-arc basin, is a hydrocarbon source that should be taken into account in models explaining gas distribution and the formation of the bottom-simulating reflector within the Kumano fore-arc basin.

Components: 6600 words, 6 figures, 2 tables.

Keywords: gas saturation; sonic data; porosity; clay mineralogy; Kumano fore-arc basin; NanTroSEIZE.

Index Terms: 7299 Seismology: General or miscellaneous; 8169 Tectonophysics: Sedimentary basin processes; 3004 Marine Geology and Geophysics: Gas and hydrate systems.

Received 13 July 2010; **Revised** 22 November 2010; **Accepted** 30 November 2010; **Published** 28 January 2011.

Doan, M.-L., M. Conin, P. Henry, T. Wiersberg, D. Boutt, D. Buchs, D. Saffer, L. C. McNeill, D. Cukur, and W. Lin (2011), Quantification of free gas in the Kumano fore-arc basin detected from borehole physical properties: IODP NanTroSEIZE drilling Site C0009, *Geochem. Geophys. Geosyst.*, *12*, Q0AD06, doi:10.1029/2010GC003284.

Theme: Mechanics, Deformation, and Hydrologic Processes at Subduction Complexes, With Emphasis on the Nankai Trough Seismogenic Zone Experiment (NanTroSEIZE) Drilling Transect

Guest Editors: D. Saffer, P. Henry, and H. Tobin

1. Introduction

[2] Porosity is a key factor for understanding the compaction and diagenesis of basin sediments [*Aagaard and Jahren*, 2010]. In situ porosity is commonly derived from sonic velocities [*Mavko et al.*, 1998]. However, interpretation of the sonic properties of clays is complex, because clays have two kinds of water storage: water bound to the clay mineral and water contained in intergranular voids. How each kind of porosity contributes to sonic velocity is unclear [*Avseth et al.*, 2005]. To better understand the relationship between clay porosities and clay sonic properties, we combine core and high-quality logging data acquired during the Integrated Oceanic Drilling Program (IODP) Expedition 319 at Site C0009, within the Kumano fore-arc basin, offshore the Kii Peninsula, Japan.

[3] Expedition 319 was conducted as part of the Nankai Trough Seismogenic Zone Experiment (NanTroSEIZE), a coordinated, multiexpedition drilling project implemented by IODP. The NanTroSEIZE project aims to understand the formation of the Nankai fore arc and its seismogenic zone [e.g., *Kinoshita et al.*, 2006]. Extensive seismic studies conducted in advance of drilling provide evidence of gas within sediments filling the Kumano fore-arc basin (Figure 1, see also *Moore et al.* [2009]). For example, a laterally extensive horizontal bottom-simulating reflector (BSR) extends throughout the basin, marking the base of the gas hydrate stability zone. Other strong reflectors may also suggest the presence of gas accumulations in the lowermost basin sediments above the older accretionary prism (Figure 1). Site C0009 was drilled in riser mode, enabling recovery of cuttings and monitoring of mud gas for the first time in IODP history and allowing the newest logging technology to be deployed in the riser hole [*Saffer et al.*, 2009, 2010]. In particular, the Schlumberger SonicScanner™ wireline logging tool recorded shear wave velocity within the unconsolidated sediments (Figure 2), providing key data needed to quantify gas accumulations.

[4] Here we evaluate porosity and gas content in the fine-grained basin filling sediments using P wave velocity (V_p) and S wave velocity (V_s) logging data. Such porosity evaluation is an important contribution, because there were no direct porosity measurements from Site C0009, with the exception of a ~90 m thick cored interval at the bottom of the hole. We calibrate the relationship between sonic properties and clay porosities from measurements on core samples, taking into account the physical and chemical properties of the clay minerals. We

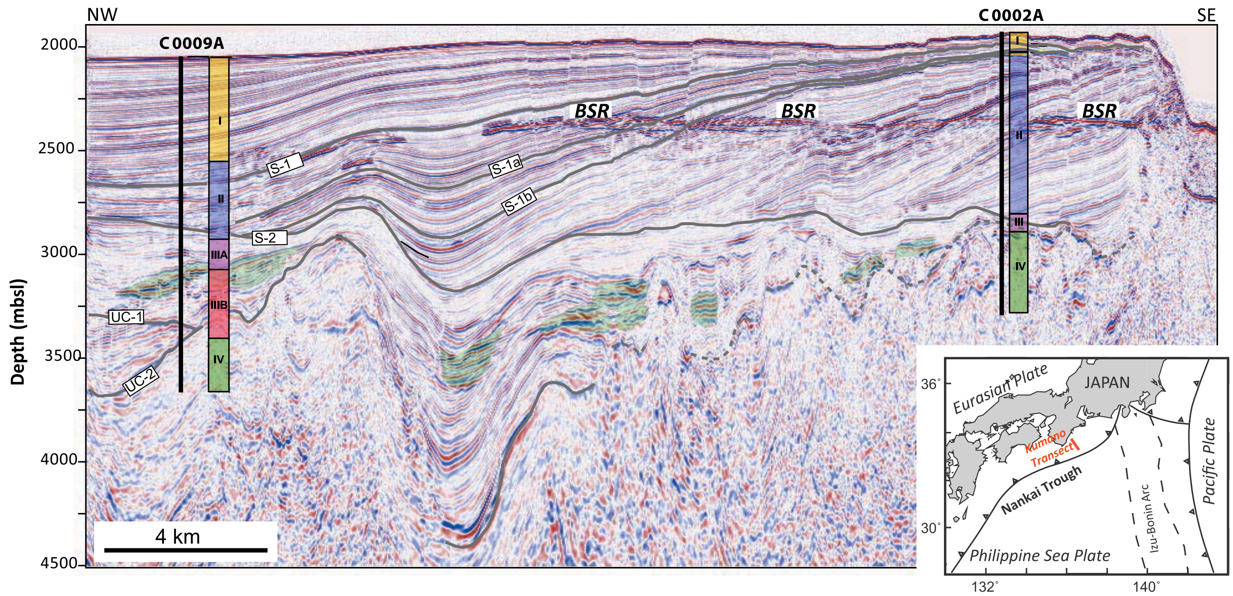

Figure 1. Seismic section across the Kumano fore-arc basin modified from *Moore et al.* [2009] and *Saffer et al.* [2010], showing the location and simplified stratigraphic columns for Sites C0009 and C0002. Possible gas pockets at the base of the basin, identified from seismic reflection images, are highlighted in green. The bottom-simulating reflector (BSR) that extends along the basin is also noted.

then perform an inversion from sonic velocity to determine porosity and water saturation. The results we obtain are consistent with other logging data, such as resistivity logs. Finally, we examine the relationship between the presence of organic matter and gas content and compare the data from Site C0009 with previously collected core and logging data from Site C0002, another IODP site drilled

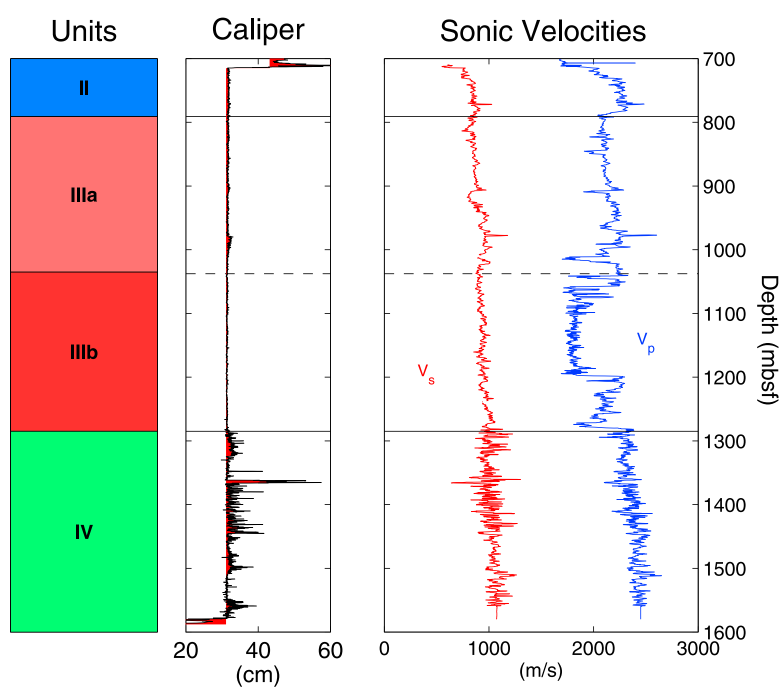

Figure 2. Sonic data from Hole C0009. In Unit IV, the data are noisier where the hole quality is degraded, as indicated by the caliper data.

15 km away, at the seaward edge of the Kumano Basin (Figure 1) [*Kinoshita et al.*, 2009].

2. Fore-Arc Basin Stratigraphy

[5] The two holes drilled within the Kumano Basin (at Sites C0002 and C0009) penetrated the thick sediments of the fore-arc basin, to total depths of 1401 m below seafloor (mbsf) and 1604 mbsf, respectively (Figure 1). Four main lithological units within the basin section were defined at Site C0009, by combining cuttings analysis with logging data [*Saffer et al.*, 2009]. These units correlate broadly with the units identified at nearby Site C0002 [*Kinoshita et al.*, 2009; *Saffer et al.*, 2010]. The four units recognized at Site C0009, from the seafloor to the bottom of the hole, are described in sections 2.1 through 2.4.

2.1. Unit I (0–467 mbsf)

[6] Although Site C0009 was drilled and cased down to 703.9 mbsf without coring or cuttings collection, a nearby 80 m deep geotechnical borehole, wireline gamma ray log measurements recorded from the seafloor during drilling and seismic profiles collectively provide good control on the nature of the shallowest drilled sediments. These data suggest that Unit I is composed of silty mudstone with cyclical sand-rich layers that range from ~10 to 50 m in thickness.

2.2. Unit II (467–791 mbsf, Upper Fore-Arc Basin)

[7] This unit is defined based on analysis of cuttings from 703.9 mbsf to 791 mbsf and logging data over its entire thickness. It is composed predominantly of unconsolidated silty mud, with silt and sand interbeds and minor interbeds of volcanic ash.

2.3. Unit III (791–1285 mbsf, Lower Fore-Arc Basin)

[8] This unit is defined on the basis of cuttings and wireline logs and is dominated by silty mudstone. The unit is subdivided into Subunits IIIa and IIIb; the boundary between the two subunits is marked by an abrupt increase in wood lignite fragments (concentrated in Subunit IIIb). Cuttings samples from within Unit III overall display a high total organic carbon (TOC) content (Figure 3), however the cuttings composition may not be representative of the average sediment [*Saffer et al.*, 2010]. Mud gas monitoring detected higher hydrocarbon concentrations from this unit relative to those above and below. In contrast, the correlated stratigraphic unit at Site C0002 is devoid of wood/lignite fragments and the TOC of the sediments is low (less than ~0.5%wt). At Site C0002, this unit is interpreted as a starved section within the early fore-arc basin or as a trench slope deposit predating formation of the fore-arc basin [*Kinoshita et al.*, 2009].

2.4. Unit IV (1285–1604 mbsf)

[9] This unit is primarily composed of consolidated silty mudstone with minor silt interbeds. The sedimentary facies resembles Unit IV at Site C0002, which was interpreted as accreted sediments (Figure 1) [*Kinoshita et al.*, 2009]. Unit IV at Site C0009 lacks the level of deformation observed in its equivalent at Site C0002 and is therefore interpreted either as a weakly deformed package of accreted trench sediments, as trench slope sediments deposited over accreted sediments of the early prism or as earliest fore-arc basin deposits [*Saffer et al.*, 2010].

3. Sonic Data

[10] The SonicScanner™ generates high-quality sonic data. It uses 3 monopole sources (2 near field, located 30.5 cm from the nearest receiver and 1 far field, located 3.353 m from the nearest receiver) and records *P* waves on an array of 13 receivers. Frequencies for the monopole emitter span 5–20 kHz. The SonicScanner™ also measures shear wave velocity in two orthogonal directions. The dipole emitters are located 4.572 m and 5.182 m from the base of the receiver arrays and the frequency range is 300 Hz–8 kHz. Figure 2 shows the azimuthally averaged sonic velocities recorded at Site C0009. Both *P* and *S* waves were recorded and identified, even in soft unconsolidated clay-dominated sediments. Unfortunately, the azimuthally averaged shear wave velocity values are the only shear wave data available for Site C0009. However, shipboard *P* wave measurements on core samples from the base of the borehole show that the seismic anisotropy is less than 5%, at a confining pressures above ~15–20 MPa (Figure 4). Therefore, we assume the medium to be nearly isotropic.

[11] Different patterns of sonic velocity are observed between Units II, III and IV (Figure 2). In Unit II, V_p and V_s increase with depth, from 1900 m/s to 2300 m/s and from 765 m/s to 900 m/s, respectively. At the top of Unit III, a decrease in sonic

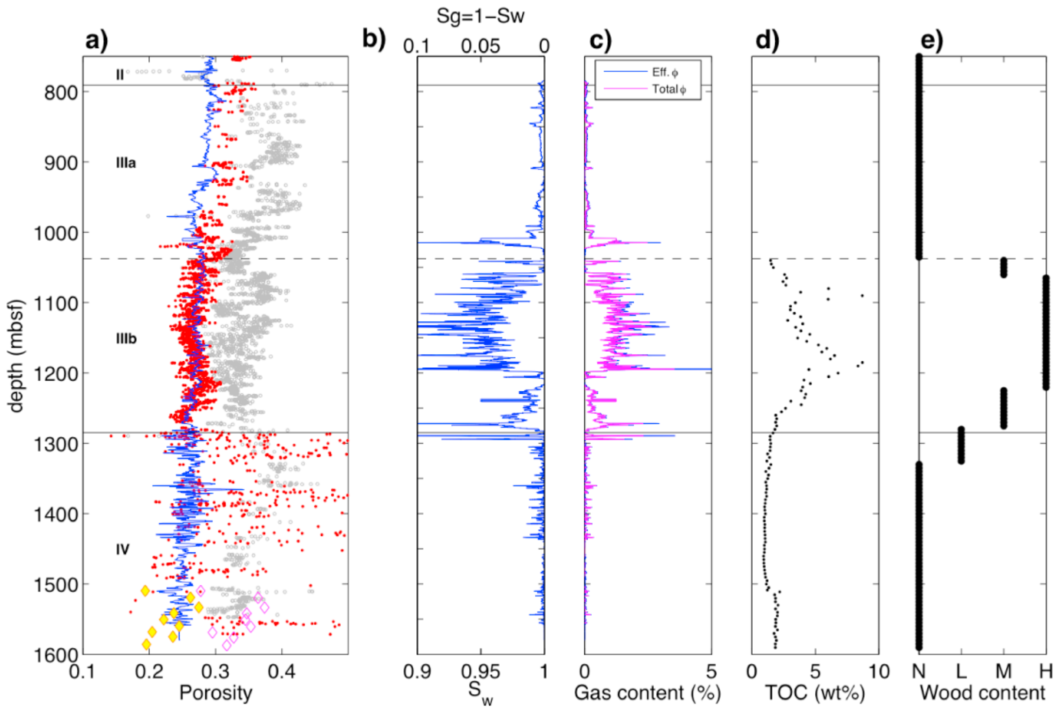

Figure 3. Results from the inversion of Brie equations (a) using the matrix parameters derived from effective porosity data (Table 1, yellow diamonds, black line in Figure 5). The corresponding porosity profile (solid blue line) is consistent with the effective porosity estimated from resistivity logs (red dots), using data with a standoff less than 0.01 in. (0.25 mm). The estimated porosity is lower than the total porosity, as computed from the lithodensity log (gray circles) or the core moisture and density (purple open diamonds). (b) Water saturation derived from effective porosity data. (c) Profile of gas content $\varphi\,(1{-}S_w)$ determined by using the effective porosity (black lines in Figure 5) and total porosity (purple lines in Figure 5). Both inversions yield the same free gas content. (d) Total organic carbon (TOC) content determined from analysis of the cuttings. (e) Wood content abundance determined from visual inspection of cuttings during Expedition 319 [*Saffer et al.*, 2010]. (N, no presence; L, low content; M, medium content; H, high content).

velocity, most obviously seen in the S wave data, accompanies the transition to muddier sediments. Within Unit III, both P and S wave velocities increase with depth, except in some regions where V_p drops sharply, which we interpret as a function of the presence of free gas (discussed below). Within Unit IV, the borehole experienced stability problems, with frequent occurrence of drilling-induced compressive failure (i.e., borehole breakouts [*Lin et al.*, 2010]), resulting in noisier sonic data. However, an increase in sonic velocity with depth is still distinguishable, especially in the P wave data (Figure 2).

4. Brie Equations for Clay

[12] Sonic velocities provide information on the mechanical compliance of the sediment framework. At a given effective pressure, two main factors control the P and S wave velocities of a porous medium: (1) porosity and (2) free gas within the pore fluid. To quantify both parameters, we combine elastic theory of porous media and empirical sonic data. The classical Willy model of sonic velocity does not appropriately describe the sonic properties of clay-rich sediments [*Mavko et al.*, 1998], therefore, we use an alternative model developed by *Brie et al.* [1995]. This is a semi-empirical model that takes into account the dependence of sonic velocity on porosity and water saturation. The advantage of this model is its use of a small number of coefficients. These coefficients have been validated by empirical fits to several logging data sets [*Brie et al.*, 1995].

[13] The basis of the Brie model is the Biot-Gassmann equation for porous media, which relates the bulk modulus of the fluid-filled material (K) to the modulus of the dry porous medium (K_{dry}), the

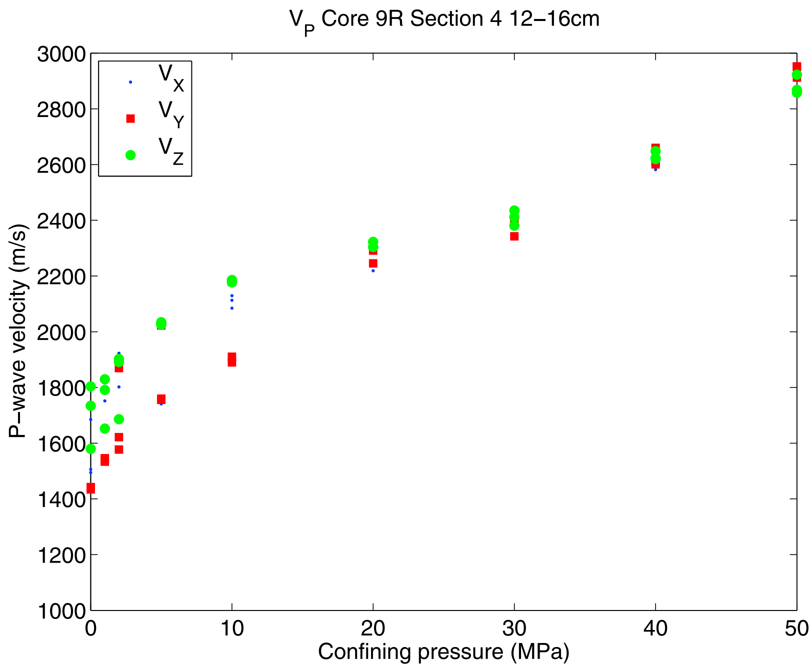

Figure 4. Shipboard *P* wave velocity data measured in section 4 of core 9 (approximate depth of 1588.5 mbsf) at several confining pressures. Core samples were first soaked in brine, covered by an impermeable layer of silicone, and then placed in a confining vessel. The *P* wave velocity was measured along the X, Y, and Z directions, where Z is oriented to the bottom of the hole and X and Y correspond to two horizontal directions. At confining pressures greater than 15–20 MPa, the samples become nearly isotropic.

bulk modulus of the solid (K_s), the modulus of the fluid (K_f) and the porosity φ:

$$K = K_{dry} + \frac{\left(1 - \frac{K_{dry}}{K_s}\right)^2}{\frac{\phi}{K_f} + \frac{1-\phi}{K_S} - \frac{K_{dry}}{K_s^2}}. \tag{1}$$

Brie et al. [1995] proposed obtaining the elastic moduli from *P* wave velocity (V_p) and *S* wave velocity (V_s),

$$\left(\frac{V_p}{V_s}\right)^2 = \frac{K}{\mu} + \frac{4}{3}, \tag{2}$$

where μ is the shear modulus of the material. Provided the material is isotropic and linear elastic, this solution holds for both dry and wet conditions and for both the porous material or solid grains by simply changing the indeces of K and μ.

[14] The theory of *Brie et al.* [1995] states that the ratio K/μ is the same for solid grains and for a porous material with pore spaces filled by a very compressible fluid,

$$\frac{K_s}{\mu_s} = \frac{K_{dry}}{\mu_{dry}}. \tag{3}$$

Brie et al. [1995] combine equation (3) with an empirical relationship,

$$\mu_{dry} = \mu_s(1-\phi)^c, \tag{4}$$

and found experimentally that the coefficient c = 8 for clays.

[15] For a water-saturated medium (without gas, S_w = 100%), higher porosity results in reduced V_p but a higher V_p/V_s ratio. In the classical $1/V_p$ versus V_p/V_s crossplot, curves similar to the solids lines (black and purple) of Figure 5 should be followed, moving toward the upper right-hand corner as porosity increases. These curves are in good agreement with the logging data collected at Site C0009.

[16] Equations (3) and (4) are the core of the theory of *Brie et al.* [1995] and are commonly used in log data analysis [*Ellis and Singe*, 2007]. Other laws can be used, such as the Hertz-Mindlin theory that derives shear and bulk moduli for a packing of similar spheres from elastic interactions at grain contacts [*Mindlin*, 1949]. However, these first-principle theories do not fit experimental data for clays, because their underlying assumptions are not satisfied. More details of alternative theories

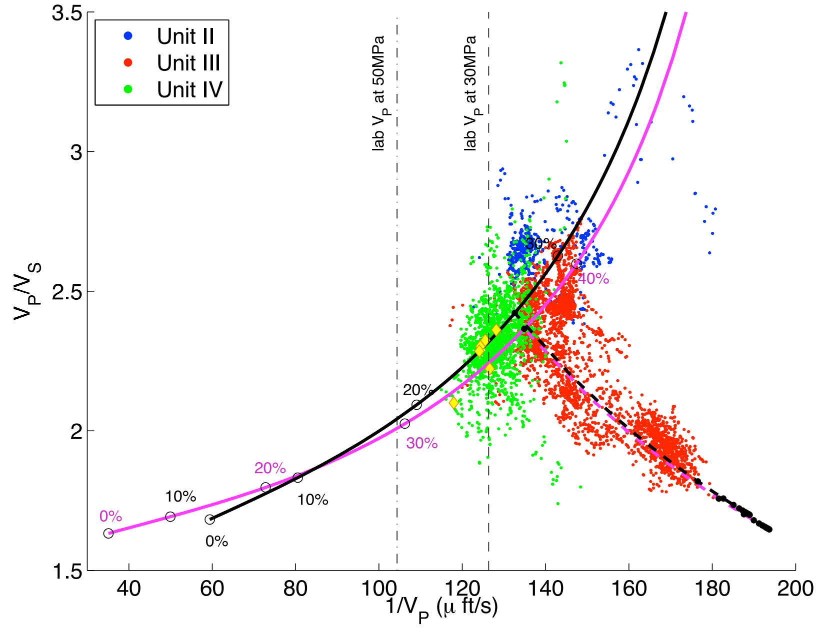

Figure 5. Crossplot of V_p/V_s ratio versus P wave slowness from sonic log data. The log data are given as point clouds. Data from Unit II are in blue, data from Unit III are in red, and data from Unit IV are in green. Among the data from Unit IV, we highlight with yellow diamonds the value of V_p and V_p/V_s obtained at depths where effective porosity was determined on core samples. The theoretical Brie curves for a fully saturated medium have been obtained using the effective porosity data (black solid line) and for the total porosity (purple solid line). Open circles indicate velocities from the Brie model for porosities of 0%, 10%, 20%, 30%, and 40%. Dashed lines show the effect of gas, assuming a porosity of 27% if using effective porosity (thick black dashed line), or 37% if using total porosity (thick purple dashed line). For reference, we also show the laboratory V_p values (see Figure 4) for a confining pressure of 30 MPa and 50 MPa.

tested during this study are provided as auxiliary material.[1]

[17] In the case of partial water saturation ($S_w < 100\%$), the fluid modulus K_f is computed as a Reuss average,

$$\frac{1}{K_f} = \frac{S_w}{K_w} + \frac{1 - S_w}{K_g}, \tag{5}$$

where K_g is the gas modulus and K_w the water modulus. In equation (5), we ignore the coupling between the fluid and the solid skeleton. At low water saturation, a meniscus forming between grain particles alters the skeleton stiffness. This effect is not incorporated into our calculations, but the high water saturation estimated from our inversion (Figure 3) confirms that this effect can safely be neglected. With more free gas, or a lower water saturation, the fluid becomes much more compliant and V_p decreases. However, shear waves do not propagate in fluids, so V_s is independent of the fluid phase filling the pores. Therefore, V_p is strongly affected by gas, whereas V_s is not (see Figure 2). The black and purple dashed lines in Figure 5 show the relationship between $1/V_p$ and V_p/V_s when water saturation varies for a given porosity. With reduced water saturation, or greater free gas content, a given data point ($1/V_p$, V_p/V_s) moves toward the lower right-hand corner.

5. Calibration of Brie Equations for Clays From IODP Site C0009

[18] Figure 5 shows SonicScanner™ log data ($1/V_p$ versus V_p/V_s) in Units II, III and IV. Units II and IV exhibit a trend typical of fully water-saturated media, but data from Unit III are shifted toward a lower V_p/V_s. This excursion is a strong indication of the presence of free gas. We use the theory of *Brie et al.* [1995] to quantify the porosity and the water saturation. We take the bulk modulus of water as equal to 2.2 GPa [*Lide*, 1991], and the gas is presumed ideal, so that its bulk modulus is presumed equal to the hydrostatic pressure and remains negligible relative to the water bulk modulus. As in the work by *Brie et al.* [1995], we assume that the

[1] Auxiliary materials are available in the HTML. doi:10.1029/2010GC003284.

coefficient c is equal to 8, as the sediments encountered at the bottom of the hole are mainly composed of clay. We also evaluated different values of the coefficient c (c = 7 and c = 9), and the results are similar for each case (Figure S2).

[19] Two key parameters still remain unknown within the Brie theory: the solid grain bulk modulus K_s and the grain shear modulus μ_s, or their equivalents, the grain P wave and S wave velocities. These two parameters are poorly known, because (1) cores were only retrieved at the bottom of the hole in a ~90 m interval within Unit IV, and (2) shipboard P wave velocity measurements made at high confining pressure do not document the properties of the solid grains, as discussed further below.

[20] The onboard P wave velocity measurements provide only a lower bound on the grain P wave velocity. After the samples were recovered from a depth of >1500 mbsf, they were soaked in brine and coated with an impermeable silicone layer. Hence, P wave velocities measured on these samples were performed under undrained conditions, in which the true effective confining pressure is now well constrained. In such conditions, the pore pressure within the sample is equal to $B\sigma_c$ where σ_c is the confining pressure, and B is the Skempton coefficient of the material, which may be as high as ~0.9 for clay [*Wang*, 2000]. The porosity of the samples at high confining pressure is therefore nonnegligible and hence the measured sonic velocity is not representative of the grain properties.

[21] Therefore, we proceeded in two stages. First, we calibrated the matrix parameters to the logging data within the cored interval. Second, we applied these parameters to the rest of the borehole. A key assumption here is that the grain properties are not affected by effective pressure. This assumption is more likely to be valid if the sediments are cemented. From the core data, we consider two kinds of porosity. In clay minerals, water can be either bound to hydrous minerals (e.g., smectite), or located in pore spaces between the grains [*Mitchell and Soga*, 2005]. Effective porosity refers to the volume of water contained only in the intergranular pore spaces [*Ellis and Singe*, 2007], whereas total porosity is the intergranular volume plus the volume of water bound to clay minerals and is computed from moisture and density (MAD) measurements [*Blum*, 1997; *Henry*, 1997]. The water bound to the hydrated minerals is a function of the number of cations present between the layers of hydrated minerals [*Ransom and Hegelson*, 1994]. The number of cations can be obtained from cation exchange capacity (CEC) measurements [*Henry*, 1997; *Bourlange et al.*, 2003; *Conin et al.*, 2008]. The effective porosity (φ_e) is expressed as

$$\phi_e = \phi_t - n \cdot \frac{m_w}{\rho_w} \cdot CEC.\rho_g \cdot (1 - \phi_t), \tag{6}$$

where φ_t is the total porosity, CEC is the cation exchange capacity (in moles per kilogram of dried sample), m_w is the water molar mass (0.018 kg.mol^{-1}), ρ_w is the water density (1024 kg.m^{-3}), ρ_g is the grain density (2650 kg.m^{-3}), and n is the average number of water molecules per cation charge.

[22] The CEC was measured by exchanging the cations with cobaltihexamine chloride [*Orsini and Remy*, 1976]. Total porosity, bound water content, and effective porosity were determined on core samples from the bottom of the borehole (Figure 3), but unfortunately cuttings samples from the rest of the borehole were not reliable for this purpose.

[23] For sediments containing swelling clay, there is some ambiguity whether the matrix in the Brie model should include the bound water and thus whether the Brie equation should be a function of the effective porosity (Table 1) or the total porosity (Table 2). For either case, the best fitting P and S wave velocities for the matrix are determined from core sample data and then used to invert the downhole sonic velocity logging data set. If we assume that the Brie equations correspond to the total porosity, the P wave velocity of the solid grains required to fit the sonic properties with the MAD porosity is ~8000 m/s, which is unrealistic. Instead, the use of effective porosity in the Brie equations results in a solid grain P wave velocity of ~5000 m/s, which is consistent with the values used by *Brie et al.* [1995]. This suggests that V_p and V_p/V_s are mostly sensitive to the intergranular pores of the sediments and to their fluid content (i.e., effective porosity), rather than to the total porosity that also includes the bound water. The values of solid grain velocities obtained from the Brie equations are then used to invert for porosity φ and water saturation S_w profiles down the borehole (Figure 3). We find that the gas saturation does not exceed 5% and that the effective porosity varies little with depth.

6. Reliability of the Inversion

[24] To check the validity of our extrapolation of data from Unit IV core samples to Unit III, we

Table 1. Core Data Used for Determining the Matrix Sonic Properties, Assuming the Brie Equations Involve the Effective Porosity, i.e., the Total Porosity Minus the Bounded Water[a]

Sample Depth (mbsf)	V_p From Log	V_p/V_s From Log	Effective Porosity From Core	Matrix P Wave (Local Inversion)	Matrix V_p/V_s (Local Inversion)	Matrix P Wave (Global Inversion)	Matrix V_p/V_s (Global Inversion)
1509.7	2584 m/s (118 s/μft)	2.10	19.4%	4486 m/s (59 s/μft)	1.64	5130 m/s (59 s/μft)	1.68
1519.2	2378 m/s (128 s/μft)	2.36	26.2%	5255 m/s (67 s/μft)	1.69		
1533.3	2408 m/s (127 s/μft)	2.22	27.5%	5733 m/s (62 s/μft)	1.60		
1541.4	2451 m/s (124 s/μft)	2.30	23.7%	4927 m/s (53 s/μft)	1.70		
1550.4	2428 m/s (126 s/μft)	2.33	22.2%	4542 m/s (58 s/μft)	1.72		
1559.7	2456 m/s (124 s/μft)	2.29	24.5%	5130 m/s (68 s/μft)	1.68		

[a]The bound water content was measured from cation exchange capacity measurements. As there are two unknowns (V_p for matrix, V_p/V_s for matrix) for two data (V_p from log, V_p/V_s from log), if we assume we know the porosity, then the inversion can be performed at each depth.

compare the computed porosities to values derived from resistivity measured along the borehole by the Schlumberger MCFL™ (Micro-Cylindrically Focused Log) tool (Figure 3a). Site C0009 was drilled with a very low resistivity mud (~0.05 Ωm) containing NaCl, KCl and NaOH. As ions are transported within the mud filtrate as it invades the formation, the invading fluid has a resistivity (R_f) about 20 times lower than the typical clay resistivity of 1 Ωm. Therefore within this invaded zone near the borehole wall, the clay surface conductivity can be neglected and effective porosity can be derived from rock resistivity (R) using Archie's law [*Archie*, 1942],

$$R = a\frac{R_f}{\phi^m}, \tag{7}$$

where a and m are chosen to equal 1 and 2, respectively, based on those computed for similar sediments drilled in the fore-arc basin at IODP Site C0002 [*Conin et al.*, 2008]. The resistivity of the invaded zone is measured with the wireline MCFL™ tool, but unfortunately poor borehole conditions prevent its use in Unit IV. As shown in Figure 3a, porosities estimated from the resistivity data agree well with the effective porosities computed from the sonic data within Unit IIIb. Within Unit IIIa, the two independent data sets exhibit similar fluctuations but are offset from each other by a few percent. Although lithologies in Units IIIa and IIIb are broadly similar, cuttings retrieved from Unit IIIa were insufficiently cohesive to allow moisture and density data measurements [*Saffer et al.*, 2010]. This may explain why the matrix sonic velocities obtained from Unit IV do not apply to Unit IIIa. Within Unit II and Unit IIIa, the correlation between porosities derived from the sonic data and those derived from resistivity logs is poor. This is likely a result of incorrect parameters within the Brie equation or an inappropriate resistivity model for the sandier lithologies present in these units. In particular, for the less consolidated sediments of Unit IIIa, the assumption that the matrix properties have little dependence on effective pressure and hence on depth is probably not valid. Matrix properties would therefore evolve with depth, and the calibration made on the cores at the bottom of the well would not be valid for Unit IIIa.

[25] Another test of the suitability of our inversion is to compute the total gas content as φ (1–S_w) (Figure 3c). As gas is not bound to clay minerals, this value should be the same for our inversion using either the total porosity or the effective porosity. The use of total porosity instead of the effective porosity in the Brie equations does not significantly

Table 2. Core Data Used for Determining the Matrix Sonic Properties, Supposing the Brie Equations Involve the Total Porosity

Sample Depth (mbsf)	V_p From Log	V_p/V_s From Log	Total Porosity From Core	Matrix P Wave (Local Inversion)	Matrix V_p/V_s (Local Inversion)	Matrix P Wave (Global Inversion)	Matrix V_p/V_s (Global Inversion)
1509.8	2580 m/s (118 s/μft)	2.08	27.8%	6541 m/s (47 s/μft)	1.58	8686 m/s (35 s/μft)	1.63
1519.6	2375 m/s (128 s/μft)	2.37	36.4%	5917 m/s (52 s/μft)	1.10		
1533.4	2405 m/s (127 s/μft)	2.22	37.4%	6865m/s (44 s/μft)	1.11		
1541.8	2418 m/s (126 s/μft)	2.27	34.7%	8580 m/s (36 s/μft)	1.65		
1550.8	2448 m/s (125 s/μft)	2.21	34.5%	5816 m/s (52 s/μft)	1.09		

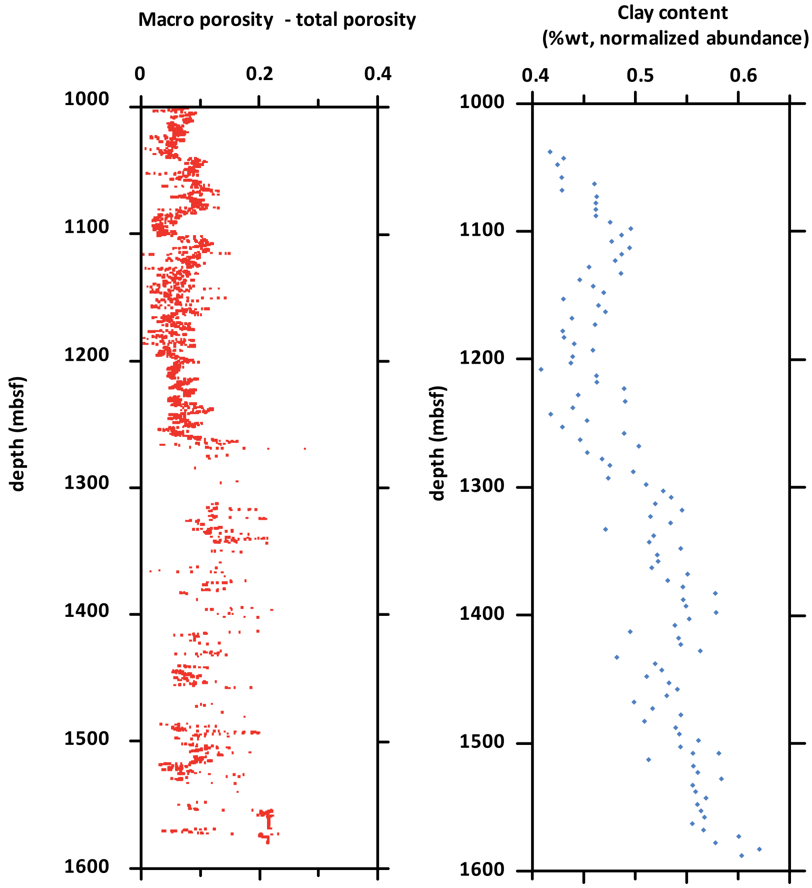

Figure 6. Comparison of water content bound to clay minerals and the total clay content from XRD analyses [*Saffer et al.*, 2010]. Bound water content is computed by differentiating the effective porosity (or macroporosity) derived from the sonic log from the total porosity derived from lithodensity log.

change the computed gas content profile (Figure 3c), exhibiting a peak of 2% of the rock volume. Thus, gas content is generally independent of matrix sonic parameters and is robustly determined by our analysis.

[26] This low gas saturation favors the use of the simple equation (5) for describing the triphasic state. In equation (5), the formation of menisci on the skeleton compliance is ignored as gas saturation was expected to be low. Our results are therefore self-consistent. From these analyses, we believe that our inverted porosities and gas contents are reliable for Units IIIb and IV.

7. Discussion

[27] The effective porosity we compute is ~10% smaller than the porosity obtained from the lithodensity log (Figure 3a). This porosity is calculated from the bulk density log (ρ_b) using the assumption of a constant grain density (ρ_g) of 2.65 g/cm^3, which is consistent with direct measurements on cuttings, and of a constant water density (ρ_w) of 1.024 g/cm^3 [*Blum*, 1997]:

$$\phi = \frac{\rho_b - \rho_g}{\rho_w - \rho_g}. \qquad (8)$$

The mass balance described by equation (8) involves the total porosity [*Brown and Ransom*, 1996], as does the calculation of core and cuttings sample porosity values from moisture and density data, which generally agree with the lithodensity log values. In Units IIIb and IV, the difference between the effective porosity (e.g., derived from the sonic log or electric resistivity log) and total porosity (e.g., derived from the lithodensity log) reflects differences in hydrous clay mineral abundance. The difference between the two porosity calculations correlates well with the total clay content measured on core samples (Figure 6), suggesting that this difference may also be related to the bound water or interlayer water of clay minerals.

[28] The gas saturation we compute ranges from ~0 to 5% (f 3b). The downhole distribution of gas appears very heterogeneous, with several zones of increased gas content. The thickest of these zones extends from 1050 mbsf to ~1200 mbsf and also includes the highest level of gas saturation. The upper extent of this zone coincides with the Unit IIIa-IIIb boundary (1037.7 mbsf) where three shallow faults dipping 3°−10° to the NW have been recognized in log images and interpreted as thrust faults [*Saffer et al.*, 2010]. The base of this zone is located at the depth of a broad maximum in total organic content (TOC), as defined from cuttings samples [*Saffer et al.*, 2010]. This correlation is consistent with the in situ production of gas from local degradation of organic matter, possibly combined with upward gas migration within Unit IIIb. Observations at Site C0009 indicate that sediments deposited in the lower Kumano fore-arc basin, beneath a regional seismic surface (interface S2, in Figure 1), are a likely source of the gas. Considering the heat flow of 40 mW/m^2 measured at nearby Site C0002 and estimated downhole temperatures of ~50°C at ~1600 mbsf at Site C0009 and < 40°C at 1200 mbsf at Site C0002 [*Kinoshita et al.*, 2009; *Saffer et al.*, 2010], gas produced at these depths is most likely biogenic.

[29] The seismically traceable layer that includes Unit III at Site C0009 and its equivalent at Site C0002 is thickest in two minibasins, one located around Site C0009 and one forming a syncline ~6 km SE of Site C0009 (Figure 1). The overlying Unit II is a sequence of muddy and sandy turbidites tilted to the north by about 5° and onlapping seismic surface S2 [*Saffer et al.*, 2010]. At Site C0002, Unit II hosts gas hydrate at the level of the BSR at about 400 mbsf. The organic matter generating the gas hydrate is likely not local to Site C0002, as neither lignite nor wood were found in the sediments of any Unit at C0002. Gas may therefore have migrated to this site to form the gas hydrate. We suggest that the gas originates from organic rich layers in the basins buried below seismic surface S2, migrates upward, and accumulates in the dipping layers of coarser sediments deposited above the seismic surface. Subsequently, the gas would migrate updip toward the southern (seaward) edge of the Kumano Basin in the vicinity of Site C0002. This may explain why the BSR displays a stronger reflectivity in the seaward part of the basin (near Site C0002) and not immediately above the deep basins further landward, near Site C0009 (Figure 1).

8. Conclusions

[30] We used high-quality sonic data obtained at Site C0009 to infer the porosity and gas saturation within the sediments of the Kumano fore-arc basin, offshore Japan. Two primary results are generated from these analyses. First, our results show that the effective porosity affects the sonic properties of the clay sediments at the bottom of the borehole (~1500 mbsf). We generate consistent results if we compare the effective porosity derived from CEC analysis on core samples, porosity estimated from the resistivity logs, and the results of our inversion of sonic log data. We also obtain good agreement between the total porosity derived from litho-density data and the total porosity from moisture and density data on core samples. As a result of these reliable and consistent data sets, we can estimate the water content stored in the intergranular porosity, a parameter otherwise difficult to obtain in a borehole with limited coring.

[31] Second, we provide further constraint on the porosity and gas saturation within the Kumano Basin sediments. We infer that a substantial amount of water, corresponding to about 10% porosity, is bound to clay minerals. The gas saturation does not exceed 5%, but this is enough to alter the *P* wave velocity profile substantially. Our inversion results show that the gas distribution is heterogeneous, but that most of the gas occurs within a lithologic unit having a high organic carbon content. This suggests that in situ bacterial gas production is the primary factor controlling free gas distribution at Site C0009 and probably within the fore-arc basin as a whole. However, the distribution of free gas and gas hydrate at the scale of the Kumano fore-arc basin suggests that gas is ultimately able to escape from the organic carbon rich layers deposited in the lower part of the basin and migrate obliquely along permeable fractures and/or dipping sand layers to shallower and more seaward parts of the basin.

Acknowledgments

[32] The authors gratefully acknowledge the support provided by the D/V *Chikyu* drilling crew, logging staff, and laboratory technicians. This work benefited from interaction with the Expedition 319 Scientific Party. We thank also the editor and an anonymous reviewer for their help with improving this

paper. This research used samples and data provided by the Integrated Ocean Drilling Program (IODP). European authors would like to thank ECORD for their support, and the French authors are furthermore grateful to INSU. The CEC measurements were made in the INRA soil laboratory of Arras.

References

Aagaard, P., and J. Jahren (2010), Special issue introduction: Compaction processes-Porosity, permeability and rock properties evolution in sedimentary basins, *Mar. Pet. Geol.*, *27*(8), 1681–1683, doi:10.1016/j.marpetgeo.2010.07.001.

Archie, G. E. (1942), The electrical resistivity log as an aid in determining some reservoir characteristics, *JPT J. Pet. Technol.*, *5*, 1–8.

Avseth, P., T. Mukerji, and G. Mavko (2005), *Quantitative Seismic Interpretation*, Cambridge Univ. Press, Cambridge, U. K., doi:10.1017/CBO9780511600074.

Blum, P. (1997), Physical properties handbook: A guide to the shipboard measurement of physical properties of deep-sea cores, *Tech. Note 26*, Ocean Drill. Program, College Station, Tex. (Available at http://www-odp.tamu.edu/publications/tnotes/tn26/INDEX.HTM)

Bourlange, S., P. Henry, J. C. Moore, H. Mikada, and A. Klaus (2003), Fracture porosity in the decollement zone of Nankai accretionary wedge using Logging While Drilling resistivity data, *Earth Planet. Sci. Lett.*, *209*, 103–112, doi:10.1016/S0012-821X(03)00082-7.

Brie, A., F. Pampuri, A. F. Marsala, and O. Meazza (1995), Shear sonic interpretation in gas-bearing sands, paper presented at 70th Annual Technical Conference and Exhibition, Soc. of Pet. Eng., San Antonio, Tex.

Brown, K. M., and B. Ransom (1996), Porosity corrections for smectite-rich sediments: Impact on studies of compaction, fluid generation, and tectonic history, *Geology*, *24*(9), 843–846, doi:10.1130/0091-7613(1996)024<0843:PCFSRS>2.3.CO;2.

Conin, M., S. Bourlange, P. Henry, and the Expeditions 314/315/316 Scientists (2008), Interpretation of LWD resistivity from Nankai accretionary wedge in the light of clay physicochemical properties, *Eos Trans. AGU*, *89*(53), Fall Meet. Suppl., Abstract T31B-1999.

Ellis, D. V., and J. M. Singe (Eds.) (2007), *Well Logging for Earth Scientists*, 2nd ed., Springer, Dordrecht, Netherlands, doi:10.1007/978-1-4020-4602-5.

Henry, P. (1997), Relationship between porosity, electrical conductivity and cation exchange capacity in Barbados wedge sediments, *Proc. Ocean Drill. Program Sci. Results*, *156*, edited by T. H. Shipley, P. Blum, and J. M. Bahr, pp. 137–149, Ocean Drill. Program, College Station, Tex.

Kinoshita, M., G. Moore, R. von Huene, H. Tobin, and C. Ranero (2006), The seismogenic zone experiment, *Oceanography*, *19*(4), 28–38.

Kinoshita, M., H. Tobin, J. Ashi, G. Kimura, S. Lallemant, E. J. Screaton, D. Curewitz, H. Masago, K. T. Moe, and the Expedition 314/315/316 Scientists (2009), *Proceedings of the Integrated Drilling Program Expeditions*, vol. 314/315/316, doi:10.2204/iodp.proc.314315316.2009, Ocean Drill. Program, College Station, Tex.

Lide, D. R. (Ed.) (1991), *CRC Handbook of Chemistry and Physics*, 72nd ed., CRC Press, Boca Raton, Fla.

Lin, W., et al. (2010), Present-day principal horizontal stress orientations in the Kumano forearc basin of the southwest Japan subduction zone determined from IODP NanTroSEIZE drilling Site C0009, *Geophys. Res. Lett.*, *37*, L13303, doi:10.1029/2010GL043158.

Mavko, G., T. Mukerji, and J. Dvorkin (1998), *The Rock Physics Handbook*, Cambridge Univ. Press, Cambridge, U. K.

Mindlin, R. D. (1949), Compliance of elastic bodies in contact, *J. Appl. Mech.*, *16*, 259–268.

Mitchell, J. K., and K. Soga (2005), *Fundamentals of Soil Behavior*, 3rd ed., John Wiley, Hoboken, N. J.

Moore, G. F., et al. (2009), Structural and seismic stratigraphic framework of the NanTroSEIZE Stage 1 transect: Kumano 3D seismic survey [online], *Proc. Integrated Ocean Drill. Program Exped.*, *314/315/316*, 46 pp., doi:10.2204/iodp.proc.314315316.102.2009.

Orsini, L., and J. C. Remy (1976), Utilisation du chlorure de cobaltihexamine pour la détermination simultanée de la capacité d'échange et des bases échangeables des sols, *Sci. Sol.*, *4*, 269–275.

Ransom, B., and H. C. Helgeson (1994b), A chemical and thermodynamic model of dioctahedral 2:1 layer clay minerals in diagenetic processes: Regular solution representation of interlayer dehydratation in smectite, *Am. J. Sci.*, *294*, 449–484, doi:10.2475/ajs.294.4.449.

Saffer, D., L. McNeill, E. Araki, T. Byrne, N. Eguchi, S. Toczko, K. Takahashi, and the Expedition 319 Scientists (2009), NanTroSEIZE Stage 2: NanTroSEIZE riser/riserless observatory, *Integr. Ocean Drill. Program Prelim. Rep.*, *319*, doi:10.2204/iodp.pr.319.2009.

Saffer, D., L. McNeill, T. Byrne, E. Araki, S. Toczko, N. Eguchi, K. Takahashi, and the Expedition 319 Scientists (2010), *Pacific Equatorial Age Transect*, *Proc. Integr. Ocean Drill. Program*, *319*, doi:10.2204/iodp.proc.319.2010.

Wang, H. F. (2000), *Theory of Linear Poroelasticity with Applications to Geomechanics and Hydrogeology*, Princeton Univ. Press, Princeton, N. J.